Immobilizing Poly(vinylphenothiazine) in Ketjenblack-Based Electrodes to Access its Full Specific Capacity as Battery Electrode Material

Bärbel Tengen, Timo Winkelmann, Niklas Ortlieb, Verena Perner, Gauthier Studer, Martin Winter, Birgit Esser,* Anna Fischer,* and Peter Bieker*

Organic batteries are considered as environmentally friendly alternative to lithium-ion batteries due to the application of transition metal-free redox-active polymers. One well-established polymer is poly(3-vinyl-*N*-methylphe-nothiazine) (PVMPT) with a fast reversibility of the electrochemical redox reaction at a potential of 3.5 V versus Li|Li$^+$. The oxidized PVMPT is soluble in many standard battery electrolytes, which diminishes its available specific capacity but at the same time can lead to a unique charge/discharge mechanism involving a redeposition process upon discharge. Herein, the influence of different conductive carbon additives and their properties, e.g., specific surface area, pore size distribution, and electrical conductivity, on the dissolution behavior of oxidized PVMPT is investigated. Compared to the state-of-the-art conductive carbon Super C65 employed in many organic battery electrodes, Ketjenblack EC-300J and EC-600J reduce the dissolution of the oxidized PVMPT due to better immobilization on the carbon additive and in the resulting 3D structure of the electrode, as assessed by N$_2$-physisorption, electrochemical, UV–vis spectroscopy and scanning electron microscopy investigations. The studies demonstrate that a dense packing of the carbon particles in the electrode is decisive for the stable immobilization of PVMPT while maintaining its long-term cycling performance.

1. Introduction

Annually the demand for energy storage systems increases, however, at the same time the urge for a sustainable and conscious lifestyle is getting more and more important for everyone. This lifestyle will rely on electrochemical energy storage systems for transportation, for storage of renewables as well as many other application areas.[1] The lithium-ion battery (LIB) is the state-of-the-art energy storage system in electric vehicles, portable devices, and further systems due to its rechargeability, high energy density, and long lifetime.[2] However, it faces many challenges regarding its components, especially in regard to the availability (also in terms of geo-political distribution) of lithium and certain transition metals, as well as the development of sustainable recycling processes.[3,4] Recycling needs to be optimized and made more efficient regarding disassembly of the cells and

B. Tengen, T. Winkelmann, V. Perner, M. Winter, P. Bieker
MEET Battery Research Center
Institute of Physical Chemistry
University of Münster
Corrensstr. 46, 48149 Münster, Germany
E-mail: peter.bieker@uni-muenster.de
B. Tengen
Faculty of Physical Chemistry, Corrensstr. 28–30 and
Center for Soft Nanoscience (SoN)
University of Münster
Busso-Peus-Str. 10, 48149 Münster, Germany
T. Winkelmann
REDcert GmbH
Schwertberger Str. 16, 53177 Bonn, Germany

The ORCID identification number(s) for the author(s) of this article can be found under https://doi.org/10.1002/adfm.202210512.

N. Ortlieb, A. Fischer
Institute of Inorganic and Analytic Chemistry
University of Freiburg
Albertstr. 21, 79104 Freiburg, Germany
E-mail: anna.fischer@ac.uni-freiburg.de
N. Ortlieb, A. Fischer
Freiburg Center of Interactive Materials and Bioinspired
Technologies (FIT)
University of Freiburg
Georges-Köhler-Allee 105, 79110 Freiburg, Germany
N. Ortlieb, B. Esser, A. Fischer
Freiburg Materials Research Center (FMF)
University of Freiburg
Stefan-Meier-Str. 21, 79104 Freiburg, Germany
E-mail: birgit.esser@uni-ulm.de
N. Ortlieb, B. Esser, A. Fischer
Cluster of Excellence livMatS
University of Freiburg
Georges-Köhler-Allee 105, 79110 Freiburg, Germany
G. Studer, B. Esser
Institute for Organic Chemistry
University of Freiburg
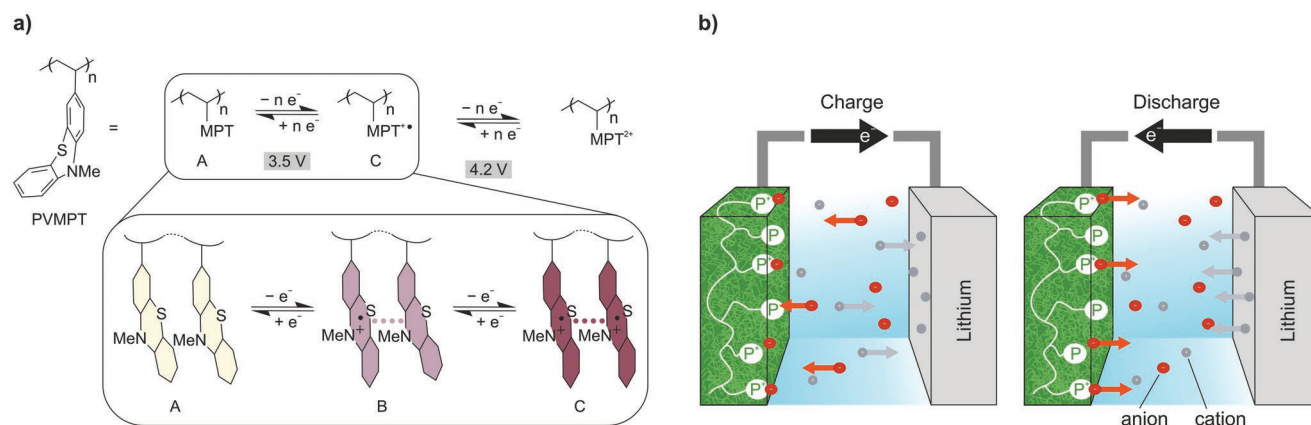Albertstr. 21, 79104 Freiburg, Germany

Figure 1. a) Redox-processes in PVMPT showing the neutral oxidation state A, the semi-oxidized state B as well as the fully oxidized state C with the π-interactions formed during cycling (reproduced with permission [18] 2017, The Royal Society of Chemistry); b) Schematic illustration of the charging and discharging process of a half-cell with a p-type redox-active polymer, e.g. PVMPT, as positive electrode and lithium metal as negative electrode based on the dual-ion principle (redrawn from ref[20,28]).

yield of the recycled materials. Due to the above-mentioned and some additional very severe ecological disadvantages, e.g., associated to the lithium and cobalt extraction for the production of LIB components, many scientists all over the world are researching for suitable alternatives to the toxic, economically critical, less environmentally friendly, and only partially abundant materials employed in LIBs.

One alternative in terms of electroactive materials are organic materials, such as redox-active polymers.[5] p-type materials with quaternary nitrogen centers[6,7] or stabilized radicals as well as organic carbonyl compounds[8] are among others the most investigated compound classes. In particular, using p-type compounds in dual-ion battery (DIB) setups often allows for fast charge/discharge rates.[9] Organic materials can be synthesized from renewable resources and can show decent specific energy and very high specific power densities.[10–14] However, due to the limited electronic conductivity of aliphatic polymer backbones with rather insulating character, in which the redox-active moieties are incorporated, electrodes based on organic redox polymers typically employ a high amount of conductive carbon such as Super C65, which negatively affects the gravimetric energy and power density. Furthermore, organic battery materials often suffer from solubility in typically applied organic solvent-based battery electrolytes.[15–17]

In this work, we analyze the redox-active polymer poly(3-vinyl-*N*-methylphenothiazine) (PVMPT), a p-type polymer with a first redox potential of 3.5 V versus Li|Li+ (**Figure 1**a). p-type materials are oxidized during charge and, thus, can be implemented as active materials at the positive electrode, i.e., the cathode during discharge (Figure 1b).[19,20] Phenothiazine is particularly

well-suited as redox-active p-type unit due to the high reversibility of its redox process and its facile functionalization chemistry.[21,22] PVMPT was first mentioned in an electrochemical context by Morishima et al.[23] in 1983. Thirty five years later, Kolek et al.[18,24] investigated the polymer as battery electrode material and discovered the underlying mechanism at the origin of the outstanding cycling stability and rate capability of PVMPT, namely π-interactions between the oxidized moieties.[18] The π-interactions take place in the oxidation state B and C (Figure 1a), between a phenothiazine radical cation and a neutral phenothiazine unit or between two radical cations. Interestingly, in many standard battery electrolytes the oxidized form C of PVMPT is soluble, while the semi-oxidized form B is only slightly soluble and redeposited on the positive electrode during discharge. For this reason and due to the high stability of the B form related to π-interactions, PVMPT-based electrodes using 1 M LiPF$_6$ in EC:DMC (1:1 by weight) as electrolyte featured only redox reactions between the oxidation states B and C during cycling, explaining that only 50% of the moieties reacted and, thus, only 50% of the theoretical specific capacity of 112 mAh g^{-1}, namely 56 mAh g^{-1}, could be achieved.[24] The dissolution of oxidized PVMPT in state C during charge and its redeposition on the positive electrode during discharge allows for structural rearrangement processes and the formation of π-interactions, which influences the cycling performance in two ways: On the one hand the accessible specific capacity is negatively affected, but, on the other hand, the π-interactions are the reason for the high cycling stability and rate capability of PVMPT due to their stabilizing effect, and because they enable hole transport. Each oxidation state (A, B, and C) could be identified by UV–vis spectroscopy measurements due to specific absorbance bands between 200 and 900 nm, which were first observed by Morishima et al.[25] in 1985. Different strategies were investigated in previous studies to prevent the dissolution of PVMPT, including changes of the electrolyte and changes within the active material itself. Perner et al.[26] investigated the application of a different electrolyte, which reduced the dissolution by a change in coordination behavior between the redox-active moieties and the solvent molecules. Furthermore, Otteny

G. Studer, B. Esser
Institute of Organic Chemistry II and Advanced Materials
Ulm University
Albert-Einstein-Allee 11, 89081 Ulm, Germany
M. Winter, P. Bieker
Helmholtz-Institute Münster
IEK-12
Forschungszentrum Jülich GmbH
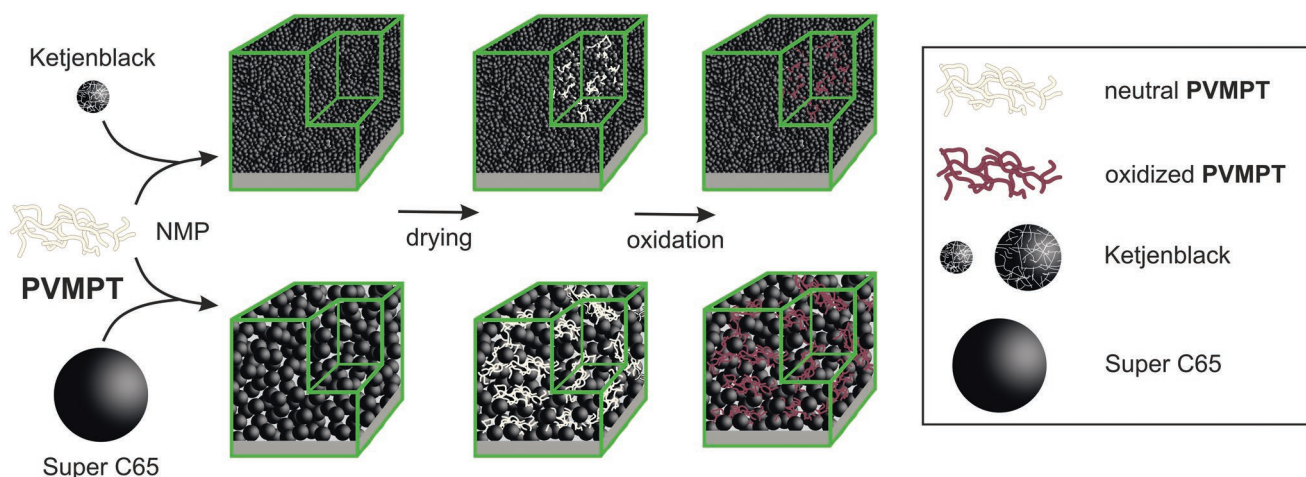Corrensstr. 46, 48149 Münster, Germany

Figure 2. Schematic illustration of the envisaged immobilization of PVMPT within the different 3D structures of the composite electrodes including conductive carbon (Ketjenblack: top row; Super C65: bottom row) and redox-active polymer material.

et al.[27] reduced the solubility of PVMPT by cross-linking the polymer to X-PVMPT, which made almost its full theoretical specific capacity accessible, but negatively affected its rate capability, since less or no specific capacity was accessible with increasing C-rates.

A third alternative to reduce the dissolution behavior of organic battery materials, in addition to changes made to the electrolyte composition and/or the redox-active polymer itself, is a variation of the conductive carbon additive employed (compared to the state-of-the-art Super C65) with the aim to encapsulate/immobilize the active material within the carbon and/or resulting 3D electrode structure and, thus, minimize the dissolution into the electrolyte.[29,30]

So far, this carbon-assisted concept has been employed primarily for the encapsulation of small redox-active organic molecules for different types of battery applications,[31–37] but remains largely unexplored for polymer-based batteries. In this context one has to consider, that while in case of small molecules encapsulation within the porous structure inside the primary carbon particles can take place (depending on the pore size), immobilization in the free space in between the primary carbon particles is more likely to occur the larger the molecular weight of the investigated redox-active polymer is.

For the first time we herein investigate whether the redox-active polymer PVMPT can be immobilized in the pores

and/or the resulting 3D structure of a composite electrode containing PVMPT as active material and different conductive carbon additives, such that the active material is electroactive and stabilized against dissolution, thereby enabling its full theoretical specific capacity to be accessible (**Figure 2**). In our study, we employed the commercially available conductive carbons Ketjenblack EC-300J and EC-600J (in the following abbreviated as KB300 and KB600) with different physicochemical properties, e.g. primary particle size, pore size, pore volume, surface functionalization, graphitization and conductivity, and an increased specific surface area in comparison to the state-of-the-art conductive carbon Super C65. KB600 and KB300 as well as Super C65 were characterized regarding their particle size by SEM, their specific surface area and pore size distribution by N_2-physisorption, and their elemental composition by elemental analysis. Additionally, Raman spectroscopy and X-ray diffraction (XRD) measurements were performed to evaluate their degree of graphitization as well as electronic conductivity. Finally, the influence of these conductive carbons as additives in PVMPT-based positive electrodes in half-cells was investigated. Mechanistic studies were performed to gain insight into the influence of the conductive carbons on the dissolution and re-deposition behavior of PVMPT during cycling. We found that the dissolution of PVMPT could be largely suppressed by using Ketjenblack carbon additives, making PVMPT's full specific
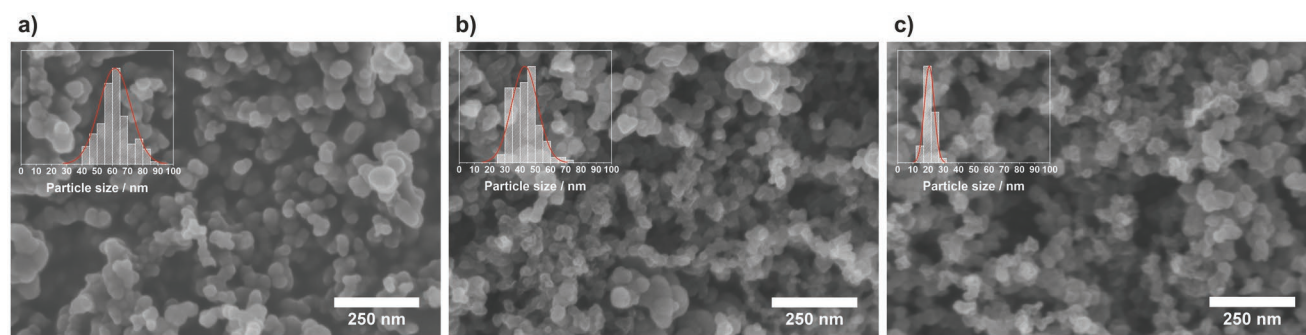

Figure 3. SEM micrographs of the conductive carbons a) Super C65, b) KB300, and c) KB600.

2210512 (3 of 14)

Table 1. Particle size, BET specific surface area and QSDFT calculated pore volume for Super C65, KB300 and KB600.

	Particle size	Specific surface area	Micropore surface area (pore size < 2 nm)		Total pore volume	Micropore volume (pore size < 2 nm)	
	[nm]	[m² g⁻¹]	[m² g⁻¹]	[%]	[cm³ g⁻¹]	[cm³ g⁻¹]	[%]
Super C65	61 ± 10	59	1.8	3.1	0.13	0.006	4.75
KB300	43 ± 9	988	45	4.5	1.19	0.189	15.9
KB600	21 ± 3	1557	44	2.8	2.54	0.193	7.60

capacity available. In addition, depending on the type of carbon additive employed, an optimum between a stable immobilization, i.e., a high specific energy, and a large capacity retention at high C-rates could be achieved, illustrating the tremendous yet fully unexplored potential of carbon additive variation, paste formulation, and electrode engineering on the performance of redox-active polymer-based battery electrodes.

2. Results and Discussion

2.1. Structure and Properties of Super C65, KB300, and KB600

To characterize the morphological, chemical and electrochemical properties of the conductive carbons, scanning electron microscopy (SEM), N_2-adsorption measurements, elemental analysis (EA), Raman spectroscopy, X-ray diffraction (XRD), and conductivity investigations were conducted. SEM measurements provided insight into the morphology/shape and primary particle size of the conductive carbons

Super C65, KB300, and KB600. In the SEM micrographs, the particles appear as spherical particles with an average particle size of (61 ± 10) nm for Super C65, (43 ± 9) nm for KB300, and (21 ± 3) nm for KB600 (**Figure 3**, **Table 1**).

N_2-adsorption measurements were conducted to investigate the specific surface areas, pore volumes and pore size distributions by applying the Brunauer–Emmett–Teller (BET) and the quenched solid density functional theory method (QSDFT, slit, cylindrical and spherical pores, N_2 on carbon, adsorption branch only). These showed that the state-of-the-art Super C65 had a specific surface area of 59 m² g⁻¹, while KB300 as well as KB600 had significantly larger specific surface areas of 988 m² g⁻¹ and 1557 g² m⁻¹, respectively, which is in good agreement with the literature.[38,39] The adsorption isotherms (**Figure 4**a) followed type II for Super C65 and type IV with increasing hysteresis for both Ketjenblack conductive carbons. An isotherm of type II is typical for low surface area macroporous materials, whereas type IV signifies the additional presence of mesopores. The hysteresis of type IV isotherm indicates capillary condensation in mesopores.[40] The aforementioned
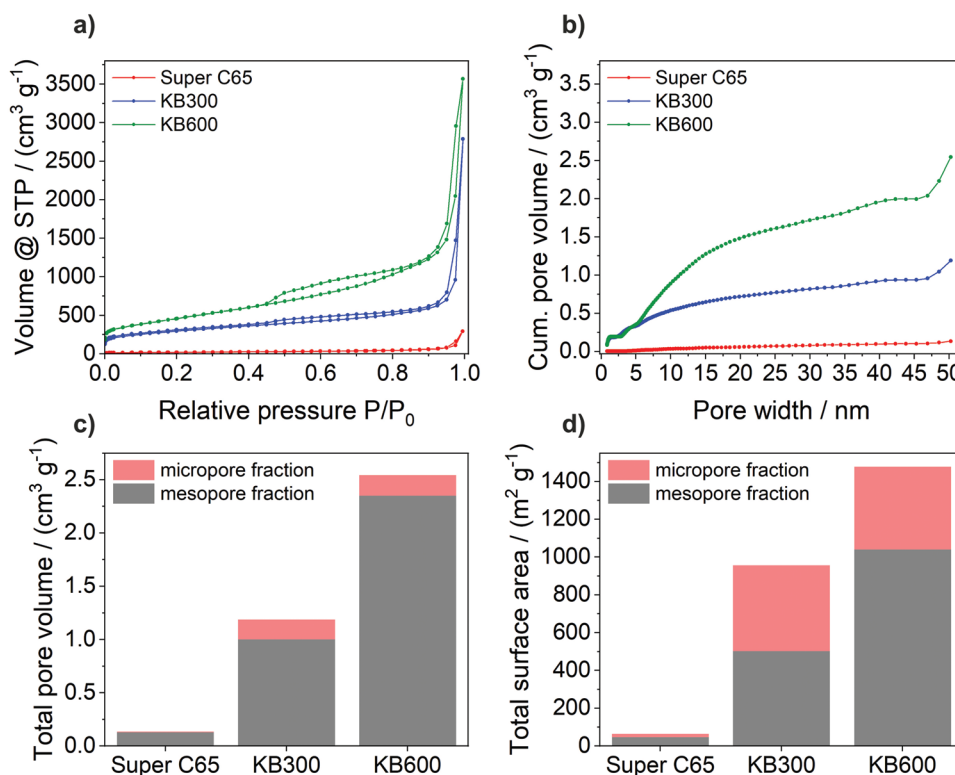

Figure 4. a) N_2-adsorption isotherms (larger representation in Figure S1, Supporting Information), b) cumulative pore volumes and c) total pore volumes as well as d) total surface area separated by micro- and mesopore volume of the conductive carbons Super C65, KB300, and KB600.
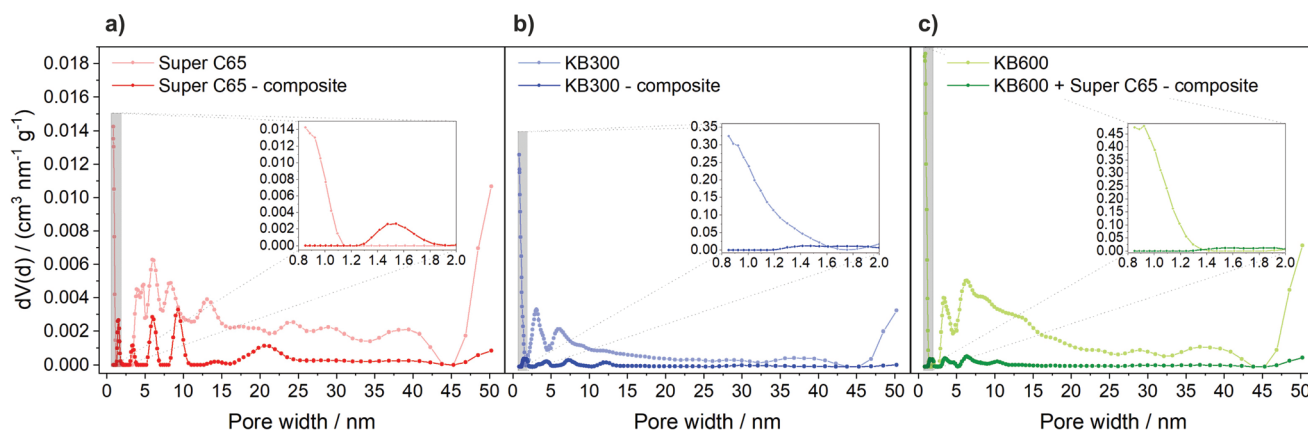
Figure 5. Pore size distributions of the conductive carbons a) Super C65, b) KB300 and c) KB600 including the average particle size; Inset: Magnification of the micropores up to 2 nm. The composites contained 50 wt.% PVMPT, 5 wt.% PVdF binder, and 45 wt.% conductive carbon (for c) 35 wt.% KB600 and 10 wt.% Super C65).

classification of the three carbons into type II and type IV isotherms is in line with the cumulative pore volume (Figure 4b), total pore volume and total surface area separated in micropore and mesopore fraction (Figure 4c,d, Table 1), as well as the pore size distribution (**Figure 5**). One must note that pores with sizes above the average particle size of the primary carbon particles most likely result from interparticle aggregation. Same is true for pores smaller but close to the primary particle size.

After applying the conductive carbons in composite materials for electrochemical measurements with 50 wt.% PVMPT and 5 wt.% PVdF binder, the same N_2-adsorption investigations (Figures S2 and S3, Supporting Information) were performed to assess the influence of the conductive carbon properties on possible interactions between the polymer and the conductive carbons. Here it is important to mention that the KB600-based composite material contained 35 wt.% KB600 and 10 wt.% Super C65 due to issues regarding the ionic and electronic conductivity of the electrodes, which was observed during the electrochemical measurements (vide infra) and has also been reported in literature.[41] After electrode paste preparation and characterization of the composite material, the specific surface areas (Table 2) were significantly reduced to 12 $m^2\,g^{-1}$, 53 $m^2\,g^{-1}$, and 74 $m^2\,g^{-1}$ for the Super C65, KB300, and KB600 conductive

carbon in PVMPT-based composite materials, respectively. This was i.a. caused by polymer filling or more likely blocking of the micropores within the carbon particles and by penetration of the mesopores present either within or between the aggregated carbon particles in the composites (Figure 2). This was further underlined by the change in pore size distribution (Figure 5) and reduced mesopore volume as well as the absence of micropores with pore widths below 1.2 nm. These results indicated that the polymer is immobilized in the 3D structure of the conductive carbon/aggregates, especially in the mesopores and, thus its dissolution could potentially be reduced.

The EAs (combustion analysis) of each carbon resulted in very similar mass contents of C-, H-, N-, and S-atoms and significant differences for the residual amount (**Figure 6**; Table S1, Supporting Information), which most likely correlates with the oxygen content in the conductive carbon. The heteroatom content has a direct influence on the hydrophilicity of the carbon support and therefore the strength of interactions between the conductive carbon particles themselves and the polymer molecules, resulting in a better immobilization and denser 3D packing of the electrode, as well as the electrolytes.

The extend of ordering, i.e., presence of graphitic structures, related to the electronic conductivity of the carbons, was

Table 2. BET specific surface areas for the conductive carbons Super C65, KB300, and KB600 in the composite, based on the whole composite mass as well as on the conductive carbon mass and QSDFT calculated pore volume for Super C65-, KB300-, and KB600-based composites.

	Specific surface area	Specific surface area – conductive carbon in composite	Micropore surface area (pore size < 2 nm)		Total pore volume	Micropore volume (pore size < 2 nm)	
	[$m^2\,g^{-1}$]	[$m^2\,g^{-1}$ conductive carbon]	[$m^2\,g^{-1}$]	[%]	[$cm^3\,g^{-1}$]	[$cm^3\,g^{-1}$]	[%]
Super C65 composite	12	27	1.1	9.2	0.021	0.001	4.8
KB300 composite	53	118	1.0	1.9	0.077	0.008	10.4
KB600 composite	74	211a)	8.1	10.9	0.156	0.007	4.5

a)normalized only to the mass of KB600, since the specific surface area of the blank Super C65 is very low in comparison and, thus, the mass of it is negligible.
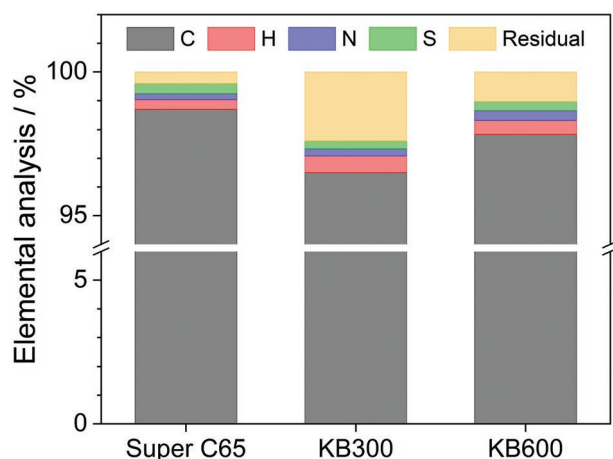
Figure 6. Elemental analysis of the conductive carbons Super C65, KB300, and KB600 (exact values in Table S1, Supporting Information).

investigated by XRD and Raman spectroscopy (**Figure 7**). The XRD diffractograms show broad reflections at $2\Theta \approx 25°$, $2\Theta \approx 43°$, and $2\Theta \approx 79°$ ($\lambda = 1.54$ Å, Cu Kα) corresponding to the graphitic (002), (100)/(101), and (110) reflections reported in literature.[42] By comparing the intensity and full width at half maximum (FWHM) of the reflections it is visible, that the main difference between the samples lays in the (002) reflection, while the rest of the diffractogram is nearly identical for all samples. This reflection corresponds to the stacking of the graphene layers within the graphitic domains. Compared to KB300 and KB600, Super C65 has a sharper and more intense (002) reflection corresponding to a higher ordering between the layers in stacking direction as well as an extended layer number in the ordered structure. At the same time, KB600 shows the broadest reflection with the lowest intensity, which translates to the lowest number and order of layers in stacking direction.

In Raman spectroscopy the obtained spectra show two broad absorption bands in the region between 1000 and 1800 cm^{-1} that were fitted by five mixed Gaussian/Lorentzian curves (Figure S4, Supporting Information). The most intense bands are the G-band at 1590 cm^{-1} and the D_1-band at 1345 cm^{-1}, which correspond to defect-free (G) and defect-rich

(D_1, edges of graphene sheets, point defects, doping, polyaromatic clusters) graphene layers. The additional three defect bands at 1620, 1530, and 1100 cm^{-1} are formed by upper layers of graphite stacks or single graphene sheets (D_2), amorphous carbon phases (D_3) and sp2 carbon bound to sp3 carbon as well as polyenes (D_4).[43,44] By comparing the intensities and FWHM of the D_1- and G-band one can obtain information about the amount of defects in the graphene structure and the in-plane size of the graphene sheets L_α. In comparison to Super C65, KB300, and KB600 show sharper D_1- and G-bands and a decrease of the amorphous D_3-band, correlating with a bigger in-plane size of graphene-like sheets. Furthermore, overtones are visible between 2400 and 3400 cm^{-1}. Again, KB300 and KB600 show sharper and more defined bands compared to Super C65, translating the more extended in-plane order within graphene-like sheets.

All in all, the three conductive carbon additives reveal very similar microstructural features with only minor differences. To finalize the characterization, the powder conductivities were determined via impedance spectroscopy in a custom build pressure cell to complement the XRD and Raman measurements (Figure S5, Supporting Information).[45] With increasing pressure (and hence particle compression) all three samples show a linear increase in electronic conductivity with values of 131 S m^{-1} for Super C65, 121 S m^{-1} for KB300 and 60 S m^{-1} for KB600 at a pressure of 1.5 MPa, which corresponds to electric resistances of 7.6, 8.2, and 16.6 mΩ m^{-1}, respectively.

As all samples show a good electronic conductivity with just minor differences in the same order of magnitude (but KB600 having the lowest conductivity), we believe that not only the electronic conductivity of the conductive carbon, but also the ionic conductivity within the electrode, in line with the 3D structure of the composite electrodes are limiting factors for the use in organic batteries (vide infra). The smaller particle size and narrower distribution of KB300 and KB600 compared to Super C65 result in a denser packing in the composite electrodes, reducing the anion diffusion and thus, ionic conductivity.[46] Therefore, the addition of Super C65 to the KB600 composite could not only increase the electrical, but also the ionic conductivity due to a less dense electrode structure induced by the addition of Super C65.
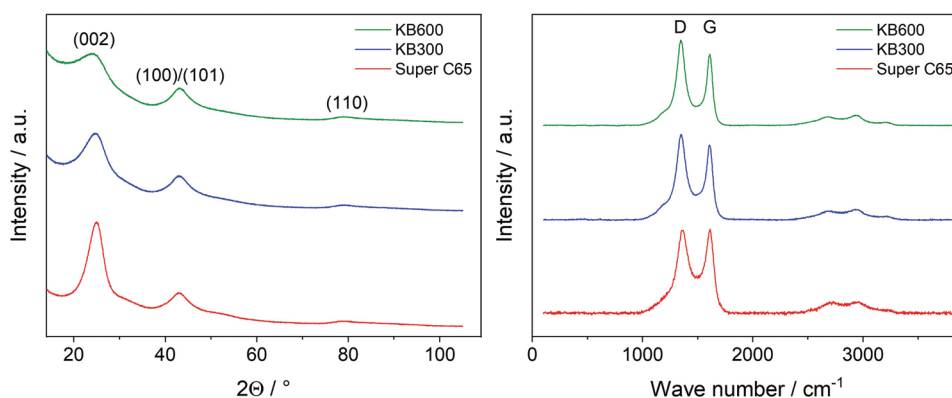

Figure 7. a) XRD pattern and b) Raman spectra normalized by peak height of the *D*-band of the conductive carbons Super C65, KB300, and KB600.
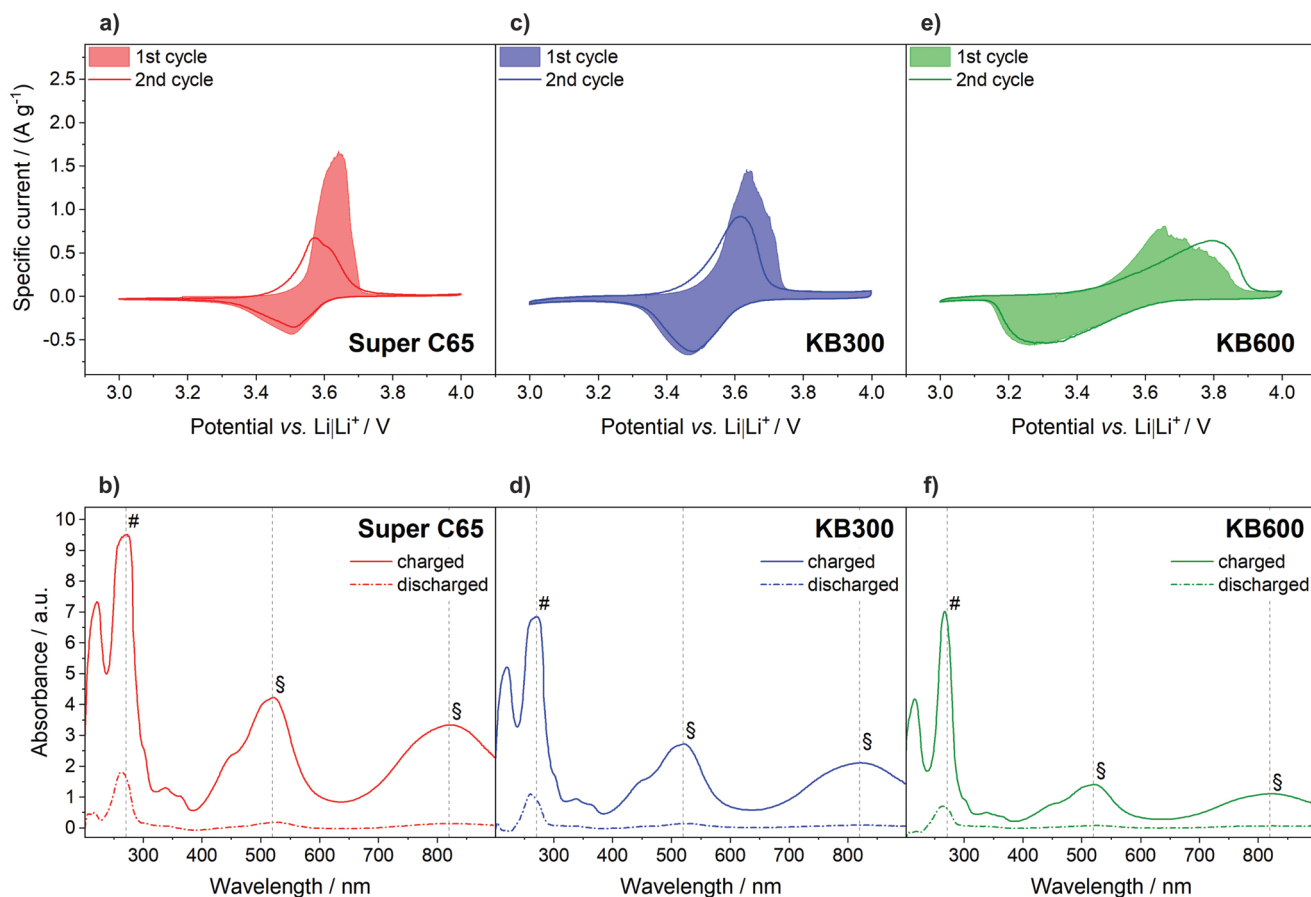
Figure 8. a,c,e) Cyclic voltammograms of PVMPT-based composite electrodes with the different conductive carbons at a scan rate of 0.5 mV s^{-1} (in Figure S8, Supporting Information the superimposition of the CV of all three conductive carbons are shown). b,d,f) Normalized UV–vis absorption spectra of electrolytes extracted from cells after one charge or charge/discharge cycle at a rate of 1 C with PVMPT-based composite electrodes with the different conductive carbons; positions of characteristic adsorption bands are indicated by # (neutral state) and § (oxidized state, 520 nm radical cation and 820 nm dimer). The electrode material contained 50 wt.% PVMPT, 5 wt.% PVdF binder, and 45 wt.% conductive carbon (for e) and f) 35 wt.% KB600 and 10 wt.% Super C65).

2.2. Electrochemical Properties of Super C65-, KB300-, and KB600-Based PVMPT Electrodes

To study the electrochemical properties of the PVMPT-based electrodes with the different conductive carbons, cyclic voltammetry (CV), constant current cycling (CCC), rate capability, and electrochemical impedance spectroscopy (EIS) as well as UV–vis spectroscopy and SEM investigations for post-mortem analyses after cycling were conducted. Using Super C65, KB300 and KB600 as conductive carbon in PVMPT-based electrodes, we fabricated composite electrodes containing 50 wt.% PVMPT, 45 wt.% conductive carbon, and 5 wt.% PVdF binder. Due to poor ionic and electronic conductivity of the KB600-based electrodes in comparison to the others, additional Super C65 was added to improve the poor electronic conductivity as well as to reduce dense electrode packing and hence improve ionic conductivity (35 wt.% KB600 and 10 wt.% Super C65).[41] SEM micrographs (Figure S6, Supporting Information) showed a homogenous and uniform distribution of the polymer with pores of 5.5 µm at the electrode surface for Super C65-based electrodes. For both KB300- and KB600-based electrodes at the

same magnification, less and smaller pores (2.1 µm for KB300 and < 1.0 µm for KB600) were observed, indicating a denser electrode structure that could lead to a lower ionic conductivity. In a three-electrode setup[47] lithium metal was applied as counter and reference electrode against PVMPT-based electrodes using 1 M LiPF$_6$ in EC:DMC (1:1 by weight) as electrolyte. Oxidized PVMPT had shown a high solubility in this electrolyte in previous studies,[18,24,26] so the influence of the conductive carbon additive on this property could be perfectly studied. The electrochemical measurements were conducted using a standard protocol for organic materials.[28]

In the resulting CVs (**Figure 8**a,c,e), different shapes of the anodic and cathodic peaks were visible depending on the conductive carbon additive employed. For the Super C65-based electrode (Figure 8a) the sharpest peak was observed in the initial oxidation at 3.64 V versus Li|Li$^+$, which represents the oxidation of PVMPT (Figure 1a) from oxidation state A to state C. Furthermore, a Coulombic efficiency of 43% and capacity retention of 53% were obtained. These values provide a good indication for the (ir) reversibility of the first oxidation as well as the dissolution behavior of the polymer.[26] Only 43% of

PVMPT was re-reduced in the cathodic scan direction after the initial oxidation, and in the second cycle only around half of the previously oxidized polymer underwent another oxidation. This shows that a significant amount of PVMPT was dissolved in the initial cycle in the electrolyte and is not accessible anymore in the following cycles. These results were underlined by UV–vis spectroscopy measurements (Figure 8b) of the electrolyte extracted from charged and discharged cells cycled at a rate of 1 C and in line with a previous study by Kolek et al.[24]. In the charged state of the Super C65-based electrode intense bands were observed, which showed that a high amount of oxidized PVMPT was dissolved in the electrolyte.

In comparison to the Super C65-based electrode, the CV of the KB300-based electrode (Figure 8c) showed broader anodic and cathodic peaks and an increased Coulombic efficiency (68%) in the initial cycle as well as capacity retention (70%) in the second cycle, which we ascribe to a reduced dissolution. This was confirmed by UV–vis spectroscopy measurements of the electrolyte extracted from a charged cell (Figure 8d). The slightly reduced intensity of the adsorption bands compared to the Super C65-based electrode correlates with a lower concentration of dissolved oxidized PVMPT. A further reduction of dissolution, indicated by UV–vis spectroscopy (Figure 8f) and CV measurements (Figure 8e), was obtained for PVMPT-based electrodes with 35 wt.% KB600 and 10 wt.% Super C65 as conductive carbon mixture in KB600-based electrodes. The oxidation and reduction peaks are much broader and more separated than for the KB300-based electrodes, and a Coulombic efficiency in the initial cycle of 88% as well as a capacity retention of 92% in the second cycle were accessible. The different shapes of the CVs and especially the larger separation between anodic and cathodic peak of the KB600-based electrode (Figure 8c) compared to the other two composites can be explained by a poorer electronic conductivity and lower anion diffusion,[48] caused by the denser 3D structure and packing of the electrode. This was also visible in the EIS measurements of uncycled cells (Figure S7, Supporting Information) from a broader semicircle, representing an increased interfacial and charge-transfer resistance for the KB600-based electrode (important values are shown in Table S2, Supporting Information). Almost

all PVMPT participated in the redox reaction and only a small amount was dissolved in the electrolyte and, thus, not reduced again to the neutral state A. The reduced dissolution was also observed in the UV–vis spectra (Figure 8f), shown by a lower intensity of the bands of the oxidized PVMPT compared to the other two composites. Furthermore, both Ketjenblack-based electrodes showed a low additional specific capacity in the CVs at potentials above 3.7 V versus Li|Li+ for KB300- (Figure 8b) and 3.9 V versus Li|Li+ for KB600-based electrodes (Figure 8e), indicating an additional capacitance originating from the electric double layer of Ketjenblack.[49,50]

The dissolution and re-deposition processes of the polymer were further investigated by SEM measurements (Figure S9, Supporting Information) of electrodes in the discharged state after one charge/discharge cycle at a rate of 1 C in comparison to the state-of-the-art electrodes with Super C65. The Super C65-based electrode showed a 3D and inhomogeneous accumulation of polymer on the electrode surface. In contrast, for the KB600-based electrode a homogenous, 2D and dense deposition of PVMPT on the electrode surface could be observed. The deposited new layer of polymer on the electrode probably also reduced the dissolution ability of further PVMPT. In subsequent cycles, it likely prevented the dissolving polymer from penetration through this dense and thick polymer layer. In terms of electrochemical behavior, the KB300-based electrode can be categorized between the Super C65- and KB600-based electrode.

Long-term cycling performance (**Figure 9**) was investigated in CCC measurements at a rate of 1 C for 500 cycles. For each conductive carbon, almost the full theoretical specific capacity of PVMPT of 112 mAh g−1 was accessible in the initial charge cycle, however, it was drastically reduced during discharge for Super C65-based electrodes (Figure 9a). Around cycle 60 the value decreased to a minimum and increased again until 42 mAh g−1 (< 50% of the theoretical value) were accessible in the 500th cycle. This behavior correlates well with the mechanism shown by Kolek et al.[18,24] In the first cycle, the full theoretical specific capacity is accessible due to the oxidation of PVMPT from state A to state C. Afterwards, the accessible specific capacity is reduced to less than 50% of
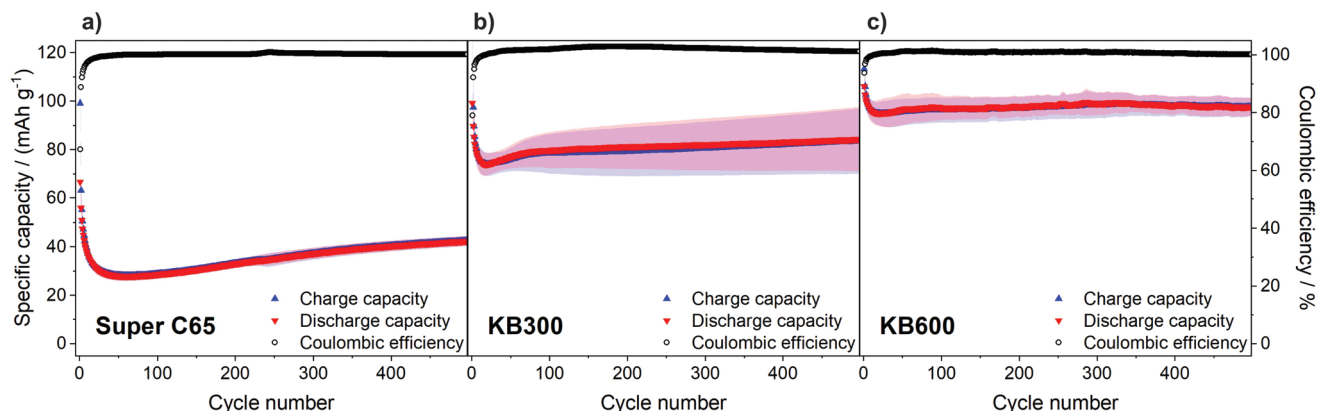

Figure 9. Constant current cycling measurements of PVMPT-based composite electrodes with a) Super C65, b) KB300 and c) KB600 as conductive carbon at a rate of 1 C between 3.0 and 4.0 V versus Li|Li+ (average of three cells shown, in Figure S10, Supporting Information, charge/discharge curves of selected cycles of all three conductive carbon-PVMPT composites are shown). The electrode material contained 50 wt.% PVMPT, 5 wt.% PVdF binder, and 45 wt.% conductive carbon (for c) 35 wt.% KB600 and 10 wt.% Super C65).
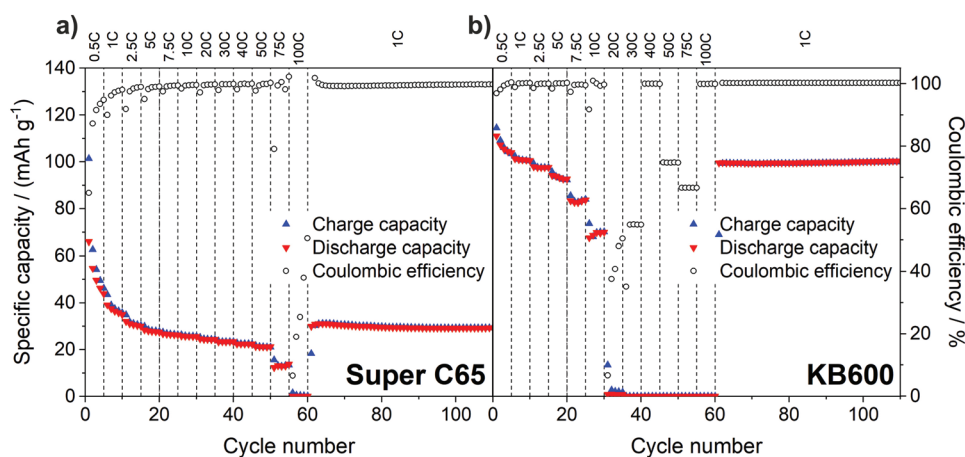
Figure 10. Rate capability investigations of PVMPT-based composite electrodes with a) Super C65 and b) KB600 as conductive carbon (in Figure S11, Supporting Information, another carbon (KB300) is shown, as well as the mean values of three cells and the differential specific capacity plots). The electrode material contained 50 wt.% PVMPT, 5 wt.% PVdF binder, and 45 wt.% conductive carbon (for b) 35 wt.% KB600 and 10 wt.% Super C65).

the theoretical value because of a dissolution of the oxidized PVMPT in oxidation state C and redeposition upon discharge to state B, involving π-interactions and the formation of a stable film. Further cycling occurs between oxidized states B and C, which correlates with a specific capacity of half (or less) of the theoretical value. A different behavior was observed for both Ketjenblack-based electrodes (Figure 9b,c). The initial drop in specific capacity was less pronounced, and for KB600-based electrodes almost no recovery in capacity was observed, as is typical for PVMPT-based electrodes (Figure 9a). Furthermore, higher values in specific capacity, namely 84 mAh g^{-1} and 97 mAh g^{-1} for the KB300- and KB600-based electrodes, respectively, were accessible in the 500th cycle, which correlate with 75% and 87% of the theoretical value of PVMPT, i.e., an increase of 95% and 126% when compared to Super C65. These high values can be explained by a better immobilization and retention of PVMPT in Ketjenblack-based electrodes. The larger surface area, reduced particle size and increased pore volumes of these carbons apparently enabled an effective immobilization in the 3D structure of the electrode, so that the dissolution of the polymer was inhibited and, thus, the accessible specific capacity increased in the sequence from Super C65-, over KB300- to KB600-based electrodes.

Due to previously mentioned issues regarding the low ionic conductivity of the electrodes based on KB600 and further research focusing on the rate capability, the rate performance of all conductive carbon-based PVMPT composites (**Figure 10**; Figure S11a,c,e, Supporting Information) from a rate of 1 to 100 C was assessed. The discharge capacities for PVMPT-based electrodes were reduced with increasing C-rate for each investigated conductive carbon. However, the overall specific capacity accessible at a rate of 1C after decreasing the C-rate again was similar to the values during CCC investigations, hence no decomposition or irreversible processes occurred, as shown in the differential specific capacity versus potential plots (Figure S11b,d,f, Supporting Information) of the C-rate investigations. For KB300- and KB600-based electrodes a capacity fading was observed starting at a rate of 75 C and 10 C, respectively, which was likely caused by slower anion diffusion due to

the lower ionic conductivity of these electrodes and the immobilization of the polymer. In theory, due to the smaller particle size of KB600, the diffusion pathways should be shorter and, thus charge/discharge cycling at higher C-rates should be facilitated, but in this case the packing of the electrode was allegedly too dense, which reduced the anion diffusion too much.[46] Considering the CCC and C-rate investigations, Super C65-based electrodes showed a high specific rate capability and KB600-based electrodes a high specific capacity. KB300 as conductive carbon in PVMPT-based electrodes represents a good compromise between these two properties.

2.3. Immobilization of PVMPT in Ketjenblack-Based Electrodes

The immobilization of PVMPT in Ketjenblack-based electrodes was further analyzed by scanning electron microscopy (SEM) and energy-dispersive X-ray analysis (EDX) measurements of cross sections of the pristine, charged and discharged KB600-based electrodes in comparison to Super C65-based electrodes. The pristine KB600-based electrode (**Figure 11**a) showed a dense particle packing without any visible diffusion channels, which underlined the poor ionic conductivity observed for these electrodes. In contrast, SEM micrographs of pristine Super C65-based electrodes showed a more porous structure with many diffusion channels (**Figure 12**a). The following EDX investigations are focused on the sulfur distribution, which mainly represents the polymer positions in the composite. Sulfur is part of the phenothiazine moiety, whereas only ≈0.3 wt.% are present in the conductive carbons according to the EA measurements (Figure 6; Table S1, Supporting Information). In the pristine KB600-based electrodes (Figure 11d) we observed an inhomogeneous sulfur distribution (further atom distributions can be found in Figure S12, Supporting Information), which is underlined by the line-scan measurements (Figure 11g; Figure S12, Supporting Information). After charging the KB600-based electrode at a rate of 1 C (Figure 11b), fractures in the composite structure were visible, which either originate from a bursting of the electrode coating
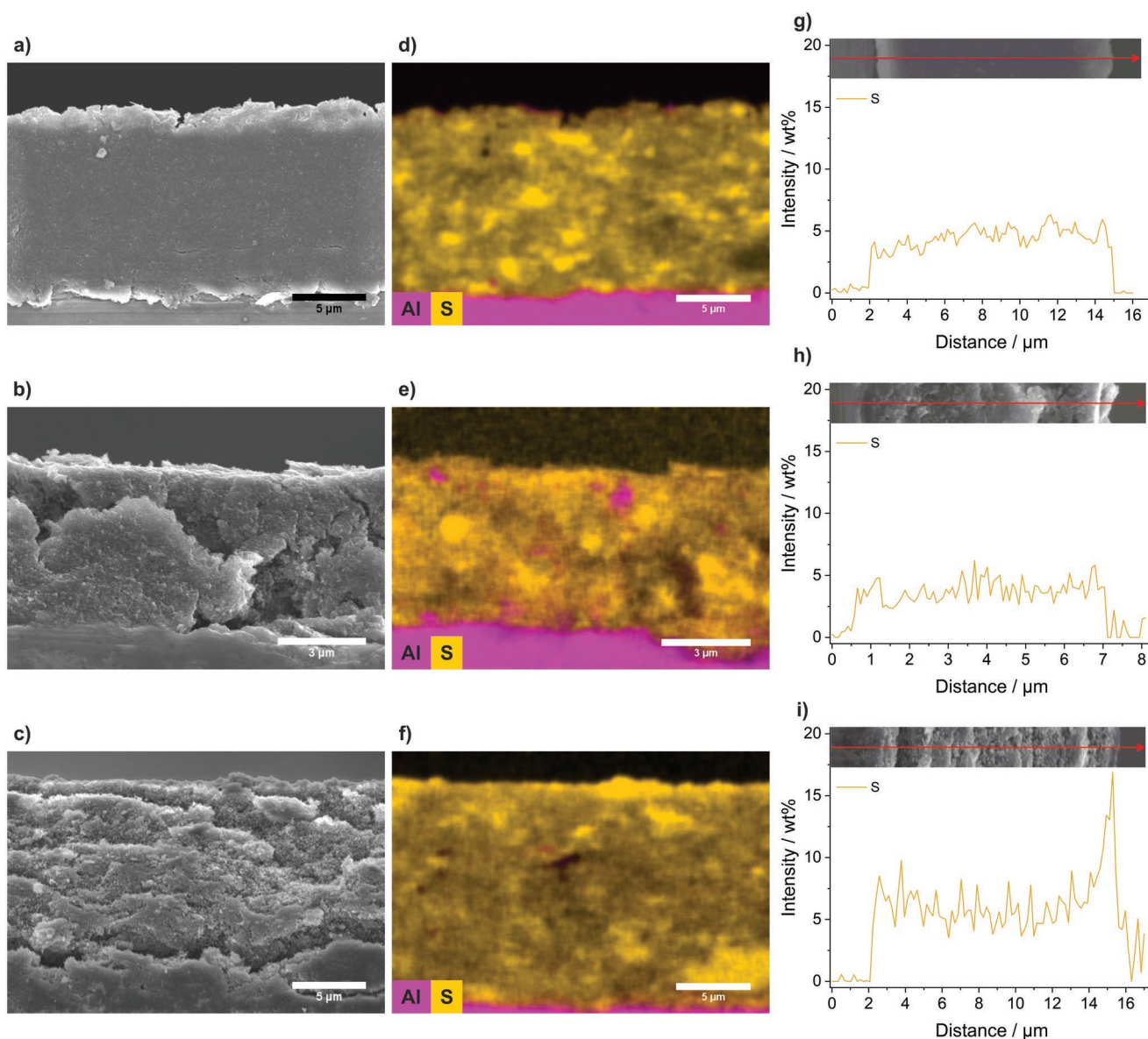
ADVANCED
SCIENCE NEWS

www.advancedsciencenews.com

ADVANCED
FUNCTIONAL
MATERIALS

www.afm-journal.de

Figure 11. Scanning electron microscopy micrographs with energy dispersive X-ray analysis (SEM-EDX) including sulfur mapping and line-scan analysis of a,d,g) pristine b,e,h) charged and c,f,i) discharged (at a rate of 1 C) PVMPT-based electrodes with 35 wt.% KB600 and 10 wt.% Super C65.

by the dissolution and passing of oxidized PVMPT or from cell disassembling. The sulfur distribution (Figure 11e) and line-scan measurements (Figure 11h; Figure S13, Supporting Information) of the charged KB600-based electrode provide a similar picture as for the pristine electrode. The S-distribution is still inhomogeneous, and no clear interpretation regarding the movement of the polymer can be made. After a full charge/discharge cycle at a rate of 1 C, similar fractures in the structure of the charged electrode were observed in the SEM micrograph of the cross-section (Figure 11c). In addition, the sulfur distribution (Figure 11f) as well as the line-scan results (Figure 11i; Figure S14, Supporting Information) showed no differences of the discharged to the charged state, solely a small accumulation of sulfur on the surface is visible after discharge, which correlates with the deposition of a small amount of PVMPT on

top of the electrode, visible in Figure S9 (Supporting Information). This behavior clearly underlined the assumption that the polymer was immobilized to a large extent in the Ketjenblack electrode and, thus, did not dissolve in the electrolyte during charging.

In contrast, Super C65-based electrodes showed a different behavior. In the EDX mapping and line-scan analysis of the pristine electrode (Figure 12d,g), an inhomogeneous sulfur distribution can be observed (further atom distributions and line-scans can be found in Figure S15, Supporting Information), similar to the KB600-based electrode. However, the more porous structure in comparison to KB600-based electrodes, visible in the SEM micrograph of the cross-section (Figure 12a), is crucial for an improved anion diffusion mentioned in the electrochemical measurements, which explains the different
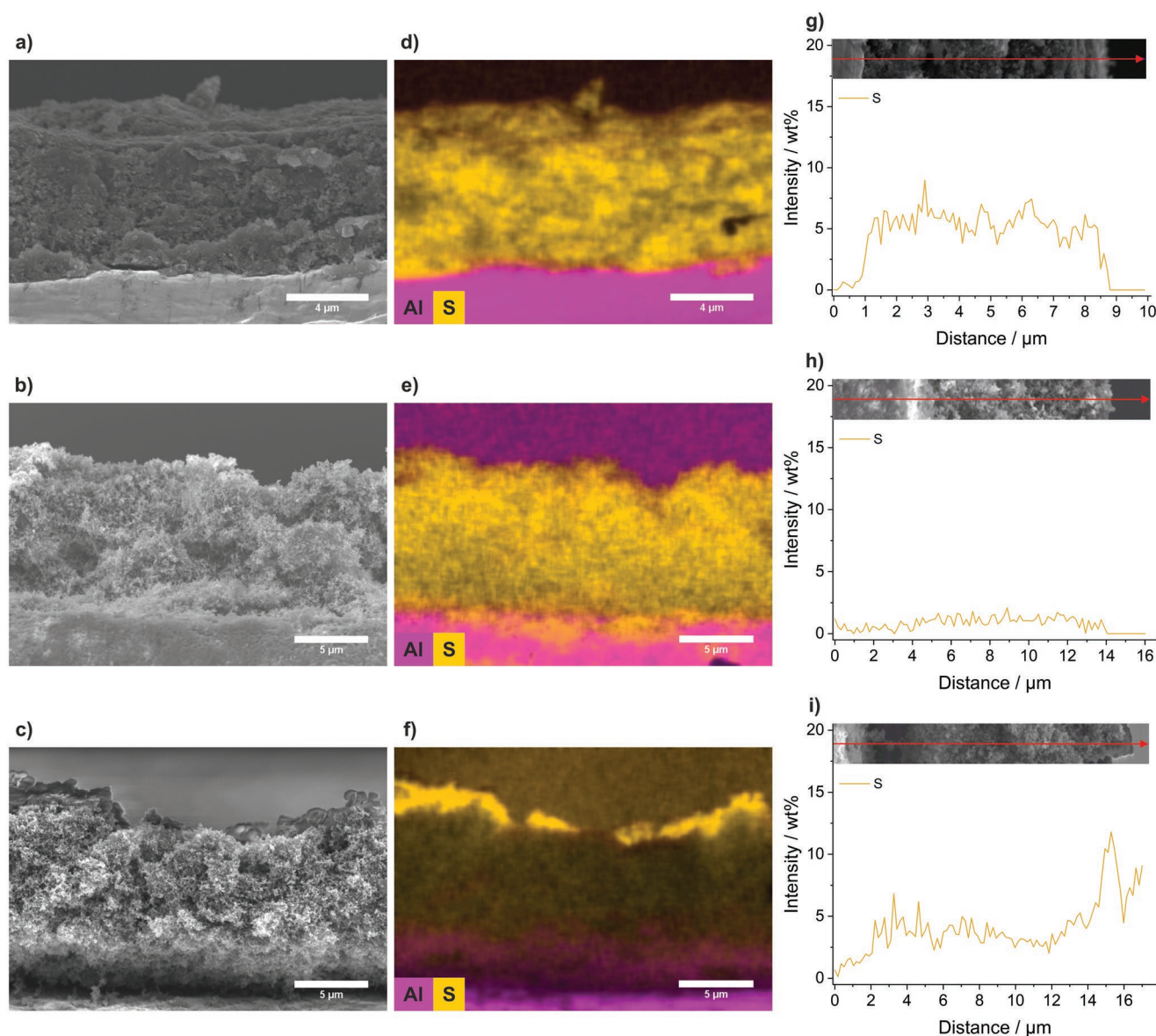
Figure 12. Scanning electron microscopy micrographs with energy dispersive X-ray analysis (SEM-EDX) including sulfur mapping and line-scan analysis of a,d,g) pristine b,e,h) charged and c,f,i) discharged (at a rate of 1 C) PVMPT-based electrodes with Super C65.

ionic conductivities. Furthermore, the charged electrode (Figure 12b) showed a more homogeneous sulfur distribution (Figure 12e) and, importantly, a significantly reduced intensity in wt.% in the line-scan (Figure 12h; Figure S16, Supporting Information). This suggests, that a reduced amount of PVMPT was present in the electrode in its charged state due to the dissolution behavior of the oxidized polymer. In the discharged Super C65-based electrode (Figure 12c), distinct depositions of PVMPT in the mapping and line-scan (Figure 12f,i; Figure S17, Supporting Information) are visible, which is also the case in the SEM micrographs of the electrode surface (Figure S9, Supporting Information). These findings demonstrate that PVMPT dissolves during charge and redeposits during discharge in Super C65-based electrodes. In KB600-based electrodes this is not the case, and PVMPT remains mostly immobilized in the electrode during charge and discharge.

Regarding the dissolution behavior of PVMPT during charge, KB300-based electrodes are somewhere in between Super C65- and KB600-based electrodes. The polymer is partly immobilized in the KB300-based electrode, so that the extent of dissolution is reduced, however, the immobilization and, thus, the hindering effect on dissolution is not as high as for KB600 with its higher surface area, higher pore volume and smaller particle size.

3. Conclusion

Our study illustrates that the type of conductive carbon additive used in the electrode formulation does have a huge influence on the performance of PVMPT-based electrodes. The positive active organic material is immobilized in electrodes based on

KB600 with its large surface area (1557 m^2 g^{-1}), micro- and mesopore volume (2.54 cm^3 g^{-1}), small primary particle size ((21 ± 3) nm) and a dense 3D structure in the composite, which effectively inhibited the dissolution of PVMPT in the battery electrolyte, so that almost its full theoretical specific capacity (97 mAh g^{-1}, corresponding to 87% of the theoretical value) was accessible. The immobilization also reduced the formation of extensive π-interactions, nevertheless, the long-term cycling performance was still highly constant. The reduced ionic conductivity of KB600-based electrodes due to denser packing without many diffusion channels and the re-deposition of a thin but dense polymer layer on top of the electrode during charge and discharge however slightly reduced the rate capability in comparison to electrodes based on the state-of-the-art Super C65. Nevertheless, by simply applying a different conductive carbon additive than the standard Super C65, in this case KB600, a higher specific capacity of PVMPT-based electrodes could be obtained. In that context, KB300-based electrodes, with KB300 having a slightly lower surface area (988 m^2 g^{-1}) and pore volume (1.19 cm^3 g^{-1}) but slightly larger particle sizes ((43 ± 9) nm) and hence less dense packed electrodes, represent a good compromise between achievable specific capacity (84 mAh g^{-1}, corresponding to 75% of the theoretical value), rate capability, cycling stability, and long-term cycling performance. In summary, our study reveals that electrode engineering bears a huge potential to optimize the performance of organic polymer-based batteries. Only by varying the conductive carbon, the properties of the active material-based electrode can be switched from high specific capacity to high specific rate capability and vice versa.

Our study makes an important contribution to the influence of conductive carbons on the performance of organic polymer-based battery electrodes. Further research will focus on immobilizing/encapsulation the polymer increasingly in the internal structure of tailored conductive carbons, i.e., in larger mesopores, and thus, achieving high-rate capability in addition to reduced solubility and thus increased accessible specific capacity. In that context, tailored carbons with specifically modifiable pore sizes but controllable particle size will allow the electrochemical properties of PVMPT-based electrodes to be further controlled and adapted for defined application purposes. This enables the existing advantages of organic materials, e.g., environmental friendliness as well as decent specific energy and very high specific power, to be retained while at the same time the weaknesses resulting from polymer solubility in the electrolyte can be overcome.

4. Experimental Section

Synthesis and Characterization of the Positive Electrode Material PVMPT: PVMPT ($M_n = 3.25 \times 10^4$ g mol^{-1}, Đ = 2.07) was synthesized as reported previously.[18]

Characterization of Blank Conductive Carbons and Composite Materials: N$_2$-physisorption isotherms were measured from 0.0005 up to 1.001 bar using an Autosorb 1-C physisorption station from Quantachrome at 77 K. Prior to the measurements, the samples were degassed under vacuum at 80 °C for 24 h. The specific surface area was determined by the Brunauer Emmett Teller (BET) method and the pore size distribution by quenched solid density functional theory (QSDFT, slit, cylindrical and spherical pores, N$_2$ on carbon, adsorption branch only) analysis using the QuadraWin software.

Elemental Analysis (C, H, N, and S) was performed using a Vario MICRO Cube System (Elementar Analysensysteme GmbH) by sample combustion at 1150 °C in O$_2$ and quantitative detection of the combustion gases (N$_2$, H$_2$O, CO$_2$, and SO$_2$).

Raman spectroscopy measurements were conducted on a Senterra II Raman microscope (Bruker Optics GmbH) with a 532 nm laser. Its power was reduced to 0.25 mW using neutral density filters and the spectra were recorded for 10 s, with 500 coadditions and a wavenumber resolution of 4 cm^{-1}.

X-ray diffraction (XRD) measurements were conducted on a Bruker D8 Discover diffractometer with Cu Kα radiation using a flat sample holder with an embedded silicon monocrystal (low background) and a rotation speed of 15 rpm. The diffractogram was recorded between 10° and 105° 2Θ with a step size of 0.025° and a measurement time of 0.5 s per step.

The electric conductivity of the conductive carbons was determined using a custom build set-up consisting of two copper stamps with a surface area of 3.85 10^{-5} m^2 and a stamp holder made of non-conductive polyether ether keton polymer (PEEK). The conductive carbon (75 mg) was placed between the copper stamps and the stamps were pressed together with 1.0, 1.5, and 2.2 MPa successively. Impedance measurements were performed for each pressure step between 1 Hz and 100 kHz at a sine amplitude of 5 mA. The resulting resistance R was converted to the specific conductivity σ using Equation (1); A_{Cu} is the surface area of the copper stamp, ρ is the bulk density of the carbon material (Super C65 160 kg m^{-1}, KB300 135 kg m^{-1}, KB600 110 kg m^{-1}), m is the used mass and R is the resistance measured.

$$\sigma = \frac{A_{Cu}\,\rho}{m\,R} \tag{1}$$

Fabrication of PVMPT-Based Electrodes

The composite electrodes were prepared using 50 wt.% PVMPT, 45 wt.% conductive carbon (Super C65, Imersy or Ketjenblack EC-300J and EC 600J, Akzo Nobel; 35 wt.% KB600 combined with 10 wt.% Super C65) and 5 wt.% binder (polyvinylidene fluoride (PVdF), Kynar Flex 761a, Arkema). PVMPT was pre-dried at 60 °C, the conductive carbons at 250 °C in a Büchi B-585 glass oven under reduced pressure (10^{-2} to 10^{-3} mbar) for 3 d. The different compounds were mixed and dispersed in NMP (N-methyl-2-pyrrolidinone, battery grade, Sigma Aldrich) until a honey-like moderate viscosity was reached. Afterward the electrode formulation was stirred at room temperature for 24 h and the resulting homogenous paste was coated onto KOH-etched aluminum foil (99.8%, Goodfellow, thickness: 20 μm) by a doctor blade (adjustable micrometer film applicator, Hohsen Corp.). The resulting wet electrode film had a thickness of 50 μm and was dried at 80 °C. Electrodes with a diameter of 12 mm were punched out with a handheld electrode punching tool (Hohsen Corp.) and further dried at 80 °C under reduced pressure (10^{-2} to 10^{-3} mbar) in a Büchi B-585 glass oven for 24 h. The dry-film thicknesses of the electrodes were measured using a digital thickness gauge (Mitutoya) by subtracting the current collector thickness from the electrode thickness and showed a value of (11 ± 3) μm (for Super C65), (8 ± 1) μm (for KB300) and (13 ± 3) μm (for KB600). The mass loadings of the active material lay between 0.19 and 0.44 mg cm^{-2} (for Super C65), 0.20 and 0.39 mg cm^{-2} (for KB300), and 0.25 and 0.42 mg cm^{-2} (for KB600).

Electrochemical Characterization and Analysis: Test cells were assembled in a dry room with less than 20 ppm humidity. Electrochemical measurements were performed in a three-electrode setup using Swagelok T-cells, except EIS measurements which were performed in a two-electrode setup using a 2032-Coin cell. Lithium foil (Albemarle, thickness: 500 μm) was used as counter (diameter: 12 mm) and reference electrode (diameter: 5 mm). In between the electrodes a six-layered pre-dried Freudenberg 2190 non-woven PP separator (FS2190), which prevents short-circuits due to lithium dendrite formation, soaked with electrolyte (1 M LiPF$_6$ in EC:DMC 1:1 by weight) was placed (13 mm diameter and 130 μL electrolyte between counter and

2210512 (12 of 14)

working electrode, 10 mm diameter and 60 µL electrolyte at reference electrode). For preparing the symmetric 2032-Coin cells the same PVMPT-based electrodes with the different conductive carbons, the 13 mm FS2190 separators and 130 µL electrolyte were applied.

Cyclic voltammetry measurements were conducted using a Swagelok T-cell with a VMP3 multi-channel potentiostat (Biologic Science Instruments) at 20 °C in a climate chamber (Binder). The cells were cycled between 3.0 and 4.0 V versus Li|Li$^+$ at a scan rate of 0.5 mV s^{-1}. The Coulombic efficiency (Equation 2) and capacity retention (Equation 3) were calculated according to the following equations;[51] $C_{Dch(n)}$ is the measured discharge capacity of cycle n, $C_{Ch(n)}$ the measured charge capacity of cycle n and $C_{Ch(n+1)}$ the measured charge capacity of cycle $n + 1$.

$$\text{Coulombic Efficiency} = \frac{C_{Dch(n)}}{C_{Ch(n)}} \quad (2)$$

$$\text{Capacity Retention} = \frac{C_{Ch(n+1)}}{C_{Ch(n)}} \quad (3)$$

Constant current cycling and *C*-rate investigations were performed using a Swagelok T-cell at 20 °C in a climate chamber (Binder) using a Maccor 4000 series battery cycler in the same potential range as cyclic voltammetry measurements. All capacities mentioned in the graphs were calculated for the amount of active material, thus, show the specific capacity and the mean of three assembled cells.

Electrochemical impedance spectroscopy measurements were conducted at a Solartron SI 1287 potentiostat in combination with a Solartron SI 1290 impedance/Gain-phase analyzer while the assembled symmetric 2032-Coin cells were stored in a climate chamber (Binder) at 20 °C. The spectra were measured at an amplitude of 5 mV in a frequency range of 1 MHz to 0.1 Hz.

Spectroscopic Measurements: UV–vis spectroscopy measurements for electrolyte investigations were conducted with a Shimadzu UV-2450 spectrometer using a sealed quartz glass cuvette (115-QS, Hellma Analytics) with a path length of 10 mm from 200 to 1100 nm. The charged and discharged battery cells were dissembled in a dry room with <20 ppm humidity and the separator soaked with the electrolyte was placed in a 1.5 mL Safe-Lock Tube (Eppendorf), containing a pipette tip as spacer. The electrolyte was extracted using a centrifuge (Mega Star 600R, VWR) at 8000 rpm for 5 min. Ten microliter of the extracted electrolyte was diluted with 400 µL of acetonitrile inside the quartz glass cuvette prior to the measurement and thoroughly shaken.

Electron Microscopic Measurements: Scanning electron microscopy measurements of the pristine and discharged electrodes were recorded on a Zeiss AURIGA CrossBeam Workstation with an in-lens detector (secondary electron (SE) detector) at a working distance of 3 to 4 mm and an acceleration voltage of 3 kV.

Scanning electron microscopy of the conductive carbons and the cross-sections were recorded on a FEG-SEM SU8220 (Hitachi) at a working distance of 3 mm as well as 5 mm and an acceleration voltage of 2 kV, respectively. For energy-dispersive X-ray measurements, an FlatQuad detector (Bruker) at a working distance of 12 mm and an acceleration voltage of 6 kV was used.

Supporting Information

Supporting Information is available from the Wiley Online Library or from the author.

Conflict of Interest

The authors declare no conflict of interest.

Author Contributions

P.B., A.F., B.E., and V.P. initiated this research. B.T., N.O., V.P., B.E., A.F., and P.B. devised the experiments and T.W. did the practical and theoretical groundwork. B.T. fabricated composite electrodes, conducted measurements in battery cells and performed electrochemical and post-mortem studies on Li-organic batteries. N.O. performed N$_2$-adsorption measurements and conducted SEM(-EDX)-cross-section, Raman spectroscopy and XRD investigations. G.S. synthesized PVMPT. M.W., B.E., A.F., and P.B. supervised the project. B.T. wrote the manuscript with input from all authors. All authors discussed and revised the manuscript and have given approval to its final version.

Data Availability Statement

The data that support the findings of this study are available from the corresponding author upon reasonable request.

Keywords

[1] C. Acar, *Int. J. Energy Res.* **2018**, *42*, 3732.
[2] A. Manthiram, *ACS Cent. Sci.* **2017**, *3*, 1063.
[3] G. Harper, R. Sommerville, E. Kendrick, L. Driscoll, P. Slater, R. Stolkin, A. Walton, P. Christensen, O. Heidrich, S. Lambert, A. Abbott, K. Ryder, L. Gaines, P. Anderson, *Nature* **2019**, *575*, 75.
[4] E. Fan, L. Li, Z. Wang, J. Lin, Y. Huang, Y. Yao, R. Chen, F. Wu, *Chem. Rev.* **2020**, *120*, 7020.
[5] P. Poizot, J. Gaubicher, S. Renault, L. Dubois, Y. Liang, Y. Yao, *Chem. Rev.* **2020**, *120*, 6490.
[6] P. Acker, M. E. Speer, J. S. Wössner, B. Esser, *J. Mater. Chem. A* **2020**, *8*, 11195.
[7] G. Dai, T. Wu, H. Chen, Y. Zhao, *Curr. Opin. Electrochem.* **2021**, *29*, 100745.
[8] H. Yang, J. Lee, J. Y. Cheong, Y. Wang, G. Duan, H. Hou, S. Jiang, I.-D. Kim, *Energy Environ. Sci.* **2021**, *14*, 4228.
[9] C. N. Gannett, L. Melecio-Zambrano, M. J. Theibault, B. M. Peterson, B. P. Fors, H. D. Abruña, *Materials Reports: Energy* **2021**, *1*, 100008.
[10] B. Esser, F. Dolhem, M. Becuwe, P. Poizot, A. Vlad, D. Brandell, *J. Power Sources* **2021**, *482*, 228814.

[11] N. Goujon, N. Casado, N. Patil, R. Marcilla, D. Mecerreyes, *Prog. Polym. Sci.* **2021**, *122*, 101449.

[12] M. D. Hager, B. Esser, X. Feng, W. Schuhmann, P. Theato, U. S. Schubert, *Adv. Mater.* **2020**, *32*, 2000587.

[13] S. Lee, J. Hong, K. Kang, *Adv. Energy Mater.* **2020**, *10*, 2001445.

[14] B. Esser, *Org. Mater.* **2019**, *1*, 63.

[15] Z. Song, H. Zhou, *Energy Environ. Sci.* **2013**, *6*, 2280.

[16] M. E. Bhosale, S. Chae, J. M. Kim, J.-Y. Choi, *J. Mater. Chem. A* **2018**, *6*, 19885.

[17] P. Acker, J. S. Wössner, G. Desmaizieres, B. Esser, *ACS Sustainable Chem. Eng.* **2022**, *10*, 3236.

[18] M. Kolek, F. Otteny, P. Schmidt, C. Mück-Lichtenfeld, C. Einholz, J. Becking, E. Schleicher, M. Winter, P. Bieker, B. Esser, *Energy Environ. Sci.* **2017**, *10*, 2334.

[19] P. Novák, K. Müller, K. S. V. Santhanam, O. Haas, *Chem. Rev.* **1997**, *97*, 207.

[20] S. Dühnen, J. Betz, M. Kolek, R. Schmuch, M. Winter, T. Placke, *Small Methods* **2020**, *4*, 2000039.

[21] P. Acker, L. Rzesny, C. F. N. Marchiori, C. M. Araujo, B. Esser, *Adv. Funct. Mater.* **2019**, *29*, 1906436.

[22] F. Otteny, G. Studer, M. Kolek, P. Bieker, M. Winter, B. Esser, *ChemSusChem* **2020**, *13*, 2232.

[23] Y. Morishima, Y. Itoh, A. Koyagi, *J. Polym. Sci., Part A: Polym. Chem.* **1983**, *21*, 953.

[24] M. Kolek, F. Otteny, J. Becking, M. Winter, B. Esser, P. Bieker, *Chem. Mater.* **2018**, *30*, 6307.

[25] Y. Morishima, I. Akihara, S.-I. Nozakura, *J. Polym. Sci. Polym. Lett.* **1985**, *23*, 651.

[26] V. Perner, D. Diddens, F. Otteny, V. Küpers, P. Bieker, B. Esser, M. Winter, M. Kolek, *ACS Appl. Mater. Interfaces* **2021**, *13*, 12442.

[27] F. Otteny, M. Kolek, J. Becking, M. Winter, P. Bieker, B. Esser, *Adv. Energy Mater.* **2018**, *8*, 1802151.

[28] S. Muench, A. Wild, C. Friebe, B. Häupler, T. Janoschka, U. S. Schubert, *Chem. Rev.* **2016**, *116*, 9438.

[29] H. Cui, P. Hu, Y. Zhang, W. Huang, A. Li, *ChemElectroChem* **2021**, *8*, 352.

[30] Y. Chen, C. Wang, *Acc. Chem. Res.* **2020**, *53*, 2636.

[31] H. Li, W. Duan, Q. Zhao, F. Cheng, J. Liang, J. Chen, *Inorg. Chem. Front.* **2014**, *1*, 193.

[32] B. Yan, L. Wang, W. Huang, S. Zheng, P. Hu, Y. Du, *Inorg. Chem. Front.* **2019**, *6*, 1977.

[33] S. Zheng, H. Sun, B. Yan, J. Hu, W. Huang, *Sci. China Mater.* **2018**, *61*, 1285.

[34] K. Zhang, C. Guo, Q. Zhao, Z. Niu, J. Chen, *Adv. Sci.* **2015**, *2*, 1500018.

[35] C. Guo, K. Zhang, Q. Zhao, L. Pei, J. Chen, *ChemComm* **2015**, *51*, 10244.

[36] Y. Yang, G. Yu, J. J. Cha, H. Wu, M. Vosgueritchian, Y. Yao, Z. Bao, Y. Cui, *ACS Nano* **2011**, *5*, 9187.

[37] Q. Zhao, Y. Hu, K. Zhang, J. Chen, *Inorg. Chem.* **2014**, *53*, 9000.

[38] M. E. Spahr, D. Goers, A. Leone, S. Stallone, E. Grivei, *J. Power Sources* **2011**, *196*, 3404.

[39] S. Maeno, *TANSO* **2006**, *222*, 140.

[40] P. Klobes, K. Meyer, R. G. Munro, *Porosity and Specific Surface Areas Measurements for Solid Materials*, NIST SP, Washington, **2006**.

[41] C. Zhang, Y. Xu, K. He, Y. Dong, H. Zhao, L. Medenbach, Y. Wu, A. Balducci, T. Hannappel, Y. Lei, *Small* **2020**, *16*, 2002953.

[42] Z. Q. Li, C. J. Lu, Z. P. Xia, Y. Zhou, Z. Luo, *Carbon* **2007**, *45*, 1686.

[43] A. Sadezky, H. Muckenhuber, H. Grothe, R. Niessner, U. Pöschl, *Carbon* **2005**, *43*, 1731.

[44] A. Y. Lee, K. Yang, N. D. Anh, C. Park, S. M. Lee, T. G. Lee, M. S. Jeong, *Appl. Surf. Sci.* **2021**, *536*, 147990.

[45] J. Sánchez-González, A. Macías-García, M. F. Alexandre-Franco, V. Gómez-Serrano, *Carbon* **2005**, *43*, 741.

[46] J. K. Mayer, H. Bockholt, A. Kwade, *J. Power Sources* **2022**, *529*, 231259.

[47] R. Nölle, K. Beltrop, F. Holtstiege, J. Kasnatscheew, T. Placke, M. Winter, *Mater. Today* **2020**, *32*, 131.

[48] R. S. Nicholson, *Anal. Chem.* **1965**, *37*, 1351.

[49] D. Tashima, K. Kurosawatsu, M. Taniguchi, M. Uota, M. Otsubo, *Elect. Eng. Jpn.* **2008**, *165*, 1.

[50] D. Tashima, H. Yoshitama, M. Otsubo, S. Maeno, Y. Nagasawa, *Electrochim. Acta* **2011**, *56*, 8941.

[51] A. Tornheim, D. C. O'Hanlon, *J. Electrochem. Soc.* **2020**, *167*, 110520.